https://doi.org/10.15302/frontphys.2026.103203

RESEARCH ARTICLE

Experimental observation of valley Hall topological waveguide based on interface engineering

Liu He[1,3,a], Shiyu Liu[2, a], Wenchao Zhai[1], Qun Ren[4], Yingying Yang[5], Yuting Yang[2, *], Jianquan Yao[3, *]

[1]Key Laboratory of Electromagnetic Wave Information Technology and Metrology of Zhejiang Province, College of Information Engineering, China Jiliang University, Hangzhou 310018, China

[2]School of Materials Science and Physics, China University of Mining and Technology, Xuzhou 221116, China

[3]Key Laboratory of Opto-Electronics Information Technology (Tianjin University), Ministry of Education, School of Precision Instruments and Opto-Electronics Engineering, Tianjin University, Tianjin 300072, China

[4]School of Electrical and Information Engineering, Tianjin University, Tianjin 300072, China

[5]Laboratory of All-Solid-State Light Sources, Institute of Semiconductors, Chinese Academy of Sciences, Beijing 100083, China

[a] These authors contributed equally to this work.

Corresponding authors. E-mail: *jqyao@tju.edu.cn, *yangyt@cumt.edu.cn

Supporting Information

Contents

1. Valley photonic crystals

There are three kinds of VPCs cell units, called as VPC1, VPC0, VPC-1 respectively, as shown in Figures S1(a1-a3). We obtain photonics band diagrams (see Figures S1(b1-b3)) in the first Brillouin zone (FBZ) by performing a numerical stimulation and calculation for cell units, from which ones can see that when rhombic unit cell composed of two alumina cylinders with an equivalence in size, Dirac cones are at the lattice high symmetry point K and K', see Figure S1(b2), once the two alumina cylinders with an inequivalence in size, Dirac cones are opened around K and K' point and form a photonics band gap. The photonic bulk bands of VPCs take place splitting at K and K' point by breaking parity-reversal symmetry (PRS) of photonic system. Although we can obtain the same bandgaps in Figures S1(b1) and (b3) based on mirror-symmetric structures (VPC1 and VPC-1), photonics states take place inversion around K and K' point for VPC1 and VPC-1, even the Berry curvatures at K and K' point take place inversion. The electric field amplitude $|E_Z|$ and phase distributions of eigenmodes are shown in right panels of Figure S1(b1), it is shown that in the first band the electric field amplitude $|E_Z|$ of eigenmodes concentrate at K point and phase winds anticlockwise respectively. In the second band all results are converse corresponding to the first band. Certainly, at K' point all results are converse corresponding to K point. Based on mirror-symmetric, in VPC-1, the counterparts are converse corresponding to VPC1, as shown in right panels of Figure S1(b3).

Based on the large separation in $\boldsymbol{k}$ space of the two valleys and the localized distribution of nonzero Berry curvature, a valley-dependent topological invariant can be defined and used to classify the topological states of the different lattices. The topological invariant is characterized by valley Chern number as

$$C_{K/K'} = \frac{1}{2\pi}\iint_{K/K'} F(\mathbf{k})d^2\mathbf{k},$$

where $F(\mathbf{k}) = \nabla_{\mathbf{k}} \times \mathrm{A}_n(\mathbf{k})$ and $\mathrm{A}_n(\mathbf{k}) = \langle \mathbf{u}_n(\mathbf{k}) | i\nabla_{\mathbf{k}} | \mathbf{u}_n(\mathbf{k}) \rangle$ are the Berry curvature and Berry connection respectively, and $\mathbf{u}_n(\mathbf{k})$ is the spatially periodic part of the Bloch function for the nth band. The integral of the Berry curvature over the FBZ is zero due to the photonic systems with time-reversal symmetry, $F(-\mathbf{k}) = -F(\mathbf{k})$, while for photonic crystal with C_3 symmetry, the Berry curvature could have nontrivial distributions around the K, K' points (i.e., valleys) of the FBZ, hence we obtain nonzero valley Chern number by integrating the Berry curvature around the K, K' points. Valley Chern number could also be referred to $C_\Delta = C_K - C_{K'}$. Integrating Berry curvatures around different valleys [错误!未找到引用源。], we further find that the valley Chern numbers are half-integers, that is, C_K=1/2 and $C_{K'}$=−1/2 for the first band, C_K=−1/2 and $C_{K'}$=1/2 for the second band. The valley Chern numbers at K and K' valleys are C_K=+1/2 and $C_{K'}$=−1/2, schematically denoted by the white "+" and "–" symbols in the right panel of Figure S1(e). The differences of the valley Chern numbers across the domain wall composed of two VPCs with mirror symmetry at the K (K') valley is $C_\Delta = \pm 1$, indicating that edge states will exist in the photonics band gap according to bulk-edge correspondence. And the group velocity direction of photonic quantum valley Hall edge states is characterized by sign of valley Chern number, at one valley there exists an interface mode with positive group velocity, whereas another one with negative group velocity exists at the other valley.

Additionally, to visualize the valley Hall topological phase transition, we numerically obtain the evolution of eigenfrequencies at the K valley for both bands as a function of δ, valley-dependent deformation. As shown in Figure S2, the obtained results confirm that the polarization of the states is flipped in the phase diagram when δ crosses zero. On the left side, LCP is below and RCP is above ($\delta < 0$) in Figure S2, but on the right side, the polarization flips to LCP above and RCP below ($\delta > 0$). This inversion indicates that there are two topologically different valley Hall phases directly related to the sign of δ. Our numerical calculations further show that the valley Chern numbers for these two valley Hall phases are exactly opposite.

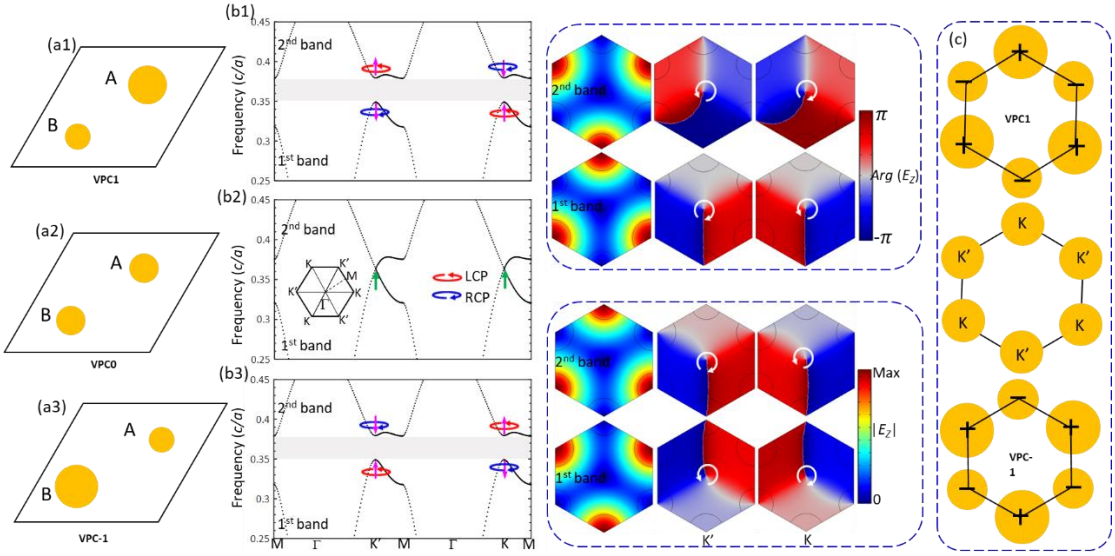

Figure S1. (a1-a3) Schematic of three kinds of VPCs cell units, VPC1, VPC0, VPC-1 respectively. (b1-b3) photonics band diagrams in the first Brillouin zone, corresponding to (a1-a3), respectively. The right panels denote the electric field amplitude $|E_Z|$ and phase distributions of eigenmodes at the K (K') valley in the first and second band respectively. (c) Schematics valley Chern numbers of distributions for VPC1, VPC-1, respectively.

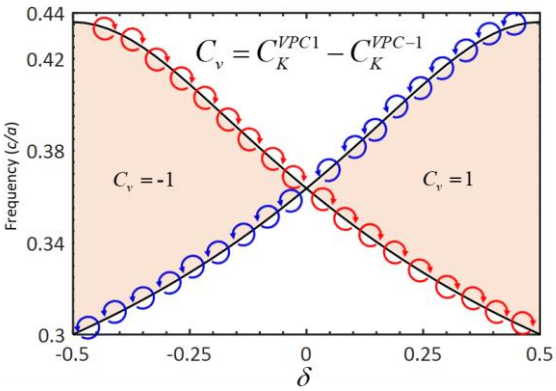

Figure S2. The evolution of eigenfrequencies at the *K* valley for both bands as a function of δ .

2. Interface type

We construct four interface types, i.e., bearded interface, comb-liked interface [1], zigzag interface, and armchair interface, respectively, where the opposite-signed δ is based on mirror-inverted symmetry. The bule lines denote interface shapes.

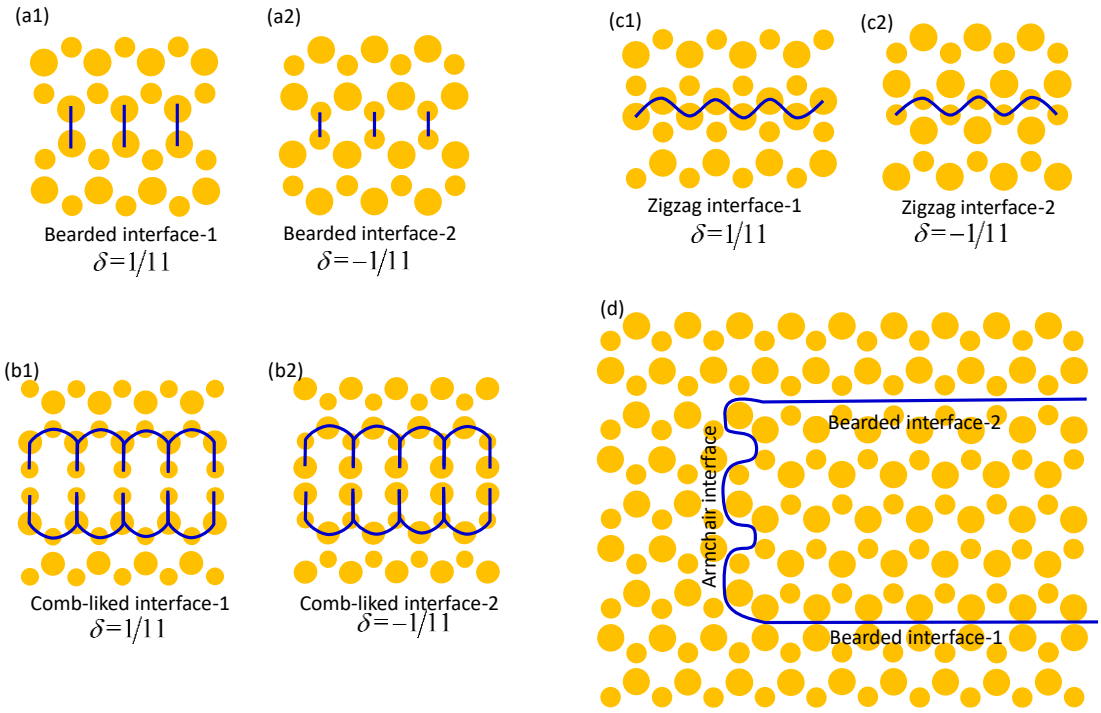

Figure S3. Schematic of interface type originating from the VPCs stacking, thereof: (a[1]) bearded interface-1, (a2) bearded interface-2, (b1) comb-liked interface-1, (b2) comb-liked interface-2, (c1) zigzag interface-1, (c2) zigzag interface-2, and (d) armchair interface, respectively.

3. Valley Hall edge states in the comb-liked interface

For comb-liked interface-1 (see Figure S4(a)), the photonic band diagram is shown in Figure S4(b). We can see that valley Hall edge states dispersion appears a fluctuation around *K* valley, namely, valley Hall edge states around *K* valley possess forward and backward group velocities, e.g., group velocity of valley Hall edge states corresponding to wavevector at left of *K* valley is positive, the other one at right of *K* valley is negative. The eigenmodes of valley Hall edge states are odd modes with regard to mid-horizontal plane, marked by blue and red dots respectively. It is worth noting that there still exist valley Hall edge states transporting one-way along the comb-liked interface-1 within special bandwidth marked by dark shadow. Further, we also demonstrate this viewpoint by observing $|E_Z|$ distributions of

valley Hall edge states in straight and Z-shaped waveguide structure, respectively, as shown in Figure S4(c) and S5(d). The bandwidth supporting valley Hall edge states with one-way transport is so narrow that valley Hall edge states appear slight backscattering due to approaching to bulk bands. Similarly, in Figure S4 (e), for $\delta < 0$, the photonic band diagram is shown in Figure S4(f). The valley Hall edge states dispersion within PBG is similar to the one shown in Fig. 2(b). The eigenmodes is not only even modes with regard to mid-horizontal plane but also is large area modes [2]. It is promising for the valley Hall edge state to achieve a kind of phase modulation [3] due to modes inversions (odd and even modes) between bearded interface-1 and comb-liked interface-2. The transmission spectra in this case are shown in Figure S4(g), showing that the unidirectional transmission in bandwidth is the highest. Full field numerical simulations of valley Hall edge states transmission are performed in straight and Z-shaped waveguide for the comb-liked interface-2 and the results are shown in Figure S4(h) and 4(i), respectively. The valley Hall edge states with large area modes, valley spin locking and robustness again sharp corners are realized in the comb-liked interface-2.

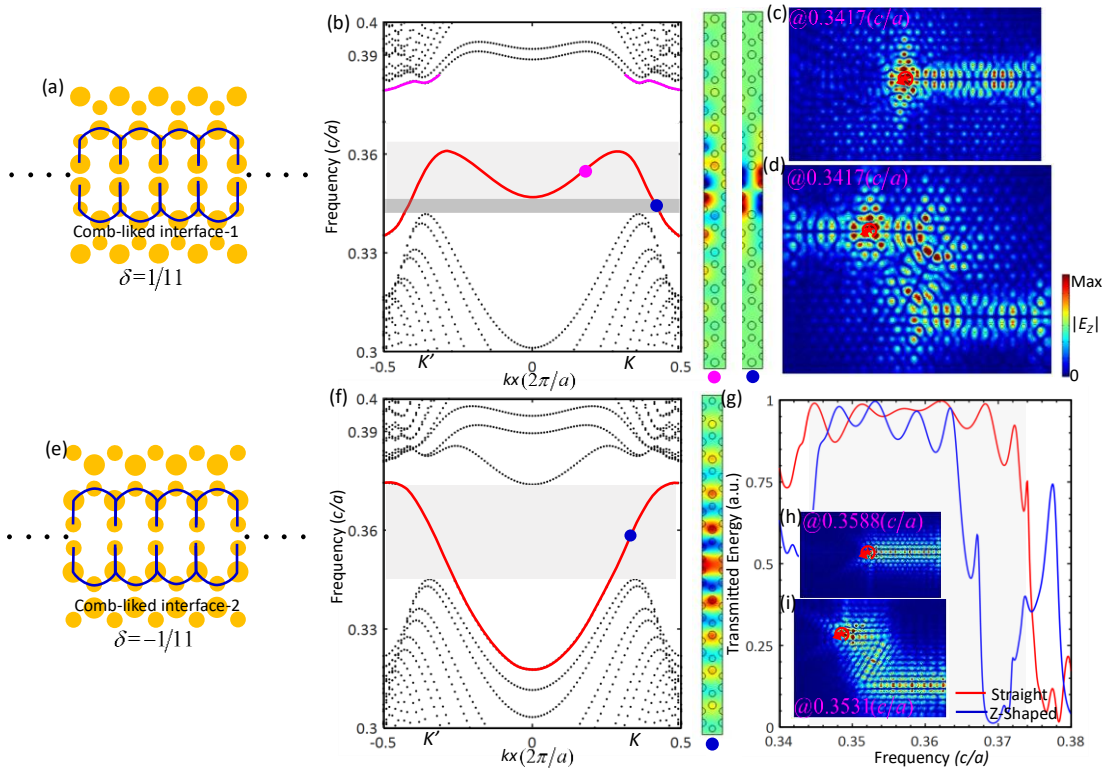

Figure S4. Valley Hall edge states in the comb-liked interface. (a) and (e) Schematic of comb-liked interface-1 and -2. (b) and (f) The photonic bulk band diagrams with comb-liked interface-1 and -2. (c) and (d) $|E_Z|$ distribution of valley Hall edge states in straight and Z-shaped waveguide for the comb-liked interface-1. (g) The transmission spectra of valley Hall edge states in straight and Z-shaped waveguide for the comb-liked interface-2. (h) and (i) $|E_Z|$ distributions of valley Hall edge states in straight and Z-shaped waveguide for the comb-liked interface-2.

4. Valley Hall edge states in the zigzag interface

For zigzag interface-1, see Figure S5(a), and the photonic band diagram is shown in Figure S5(b). We can see that valley Hall edge states dispersions marked by red curve appears a fluctuation around *K* valley, namely, valley Hall edge states around *K* valley possess forward and backward group velocities, e.g., group velocity of valley Hall edge states corresponding to wavevector at left of *K* valley is positive, the other one at right of *K* valley is negative. Hence there is in the absence of valley Hall edge states transporting one-way along the zigzag interface-1within photonics band gap marked by shadow. There are two pairs of trivial topological edge states dispersions marked by pink curve, which is gapped out from bulk bands due to breaking lattice symmetry. The right panel of Figure S5(b) shows eigenmodes of valley Hall edge states. The eigenmodes is odd modes with regard to mid-horizontal plane

corresponding to wavevector at left of K valley, marked by pink dot. The eigenmodes is even modes with regard to mid-horizontal plane corresponding to wavevector at right of K valley, marked by blue dot. There are two kinds of modes around K valley, indicating that one-way valley Hall edge states do not exist here either. Full field numerical simulations of valley Hall edge states transmission are performed and the results are shown in Figures S5(c) and S5(d), valley Hall edge states bidirectionally propagate along the zigzag interface-1 in straight and Z-shaped waveguide structure. Nonetheless, the valley Hall edge states still bypass sharp corners and maintain transport, showing that the valley Hall edge states are protected by topology. Such a topological waveguide states with bidirectional transport can be used in integrated photonics circuits with multi-channel switch and splitting.

Similarly, for $\delta < 0$, Figure S5(e) shows schematic of zigzag interface-2. The photonic band diagram is shown in Figure S5(f). The valley Hall edge states dispersion within band gap is similar to the one shown in Figure S4(b). The eigenmodes is even modes with regard to mid-vertical plane, marked by blue dot. While there are two pairs of trivial topological edge modes dispersion curves in photonics band gap. Bandwidth of trivial and nontrivial topological edge modes overlap, which will result in the edge states exhibiting trivial topology. The $|E_Z|$ distributions of valley Hall edge states in straight and Z-shaped waveguide for the zigzag interface-2 are shown in Figures S5(g) and 5(h), respectively. The edge states bidirectionally propagate along the zigzag interface-2 in straight and Z-shaped waveguide structure. However, the edge states cannot bypass sharp corners, without robustness against sharp corners or defects, showing that the edge states are trivial topological. In this case nontrivial topology of valley Hall edge states are hid.

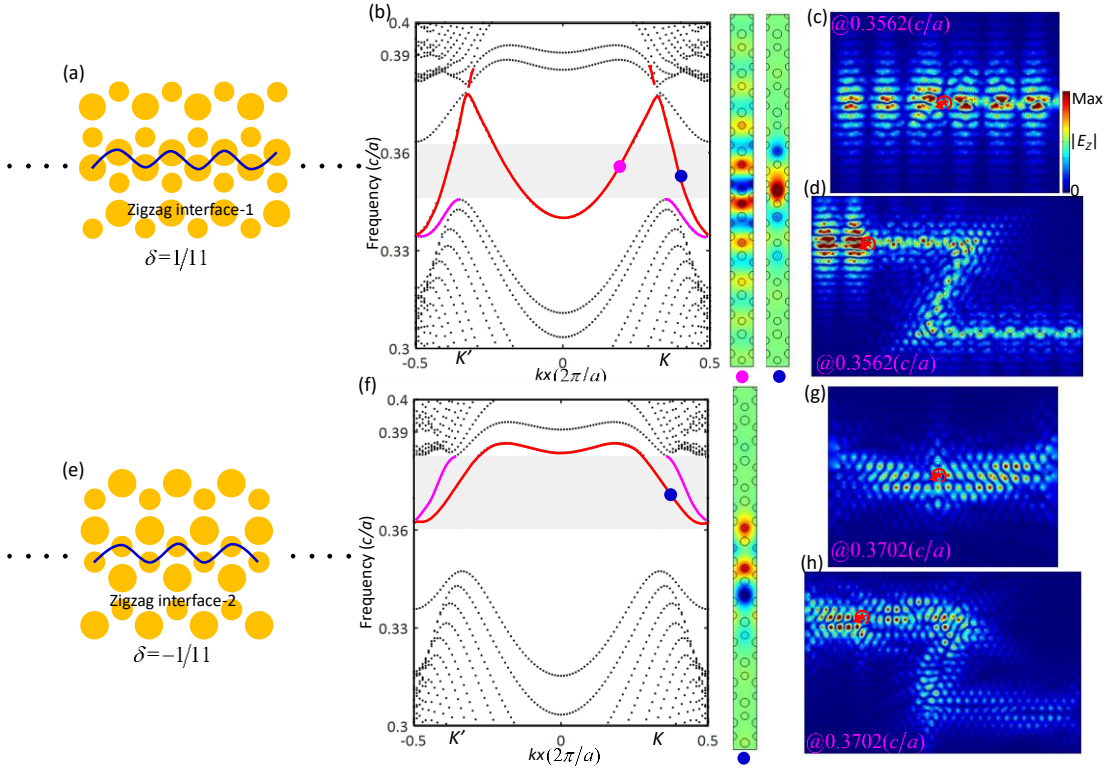

Figure S5. Valley Hall edge states in the zigzag interface. (a)and(e) Schematic of zigzag interface-1 and -2. (b) and (f) The photonic bulk bands diagrams along $\Gamma - K$ momentum space for the domain wall with zigzag interface-1 and -2. (c) and (d) $|E_Z|$ distribution of valley Hall edge states in straight and Z-shaped waveguide for the zigzag interface -1. (g) and(h) $|E_Z|$ distribution of valley Hall edge states in straight and Z-shaped waveguide for the zigzag interface-2.

5. U-shaped waveguide excited by a point source

The valley Hall edge modes dispersion curves are shown in Figures S6(a). All experimental results are shown in Figures S6(b-e), where the light source is excited by a point source in experiment. When at frequency7.58GHz corresponding to Y_1 in Figures S6(a), the valley Hall edge states one-way orderly transport along the bearded interface-2, armchair

interface and bearded interface-1, as shown in Figure S6(b). When at frequency7.68GHz corresponding to Y_2 in Figures S6(a), the valley Hall edge states one-way transport along the bearded interface-2, localizing in the interface, and enter partly armchair interface, as shown in Figure S6(c). When at frequency7.74GHz corresponding to Y_3 in Figures S6(a), the valley Hall edge states one-way transport orderly transport along the bearded interface-2, armchair interface and bearded interface-1, as shown in Figure S4(d). When at frequency7.89GHz corresponding to Y_4 in Figures S6(a), the valley Hall edge states one-way transport along the bearded interface-2 and armchair interface, localizing in armchair interface, as shown in Figure S6(e). The experiment results excited by point source are coincident with numerical simulations and analysis.

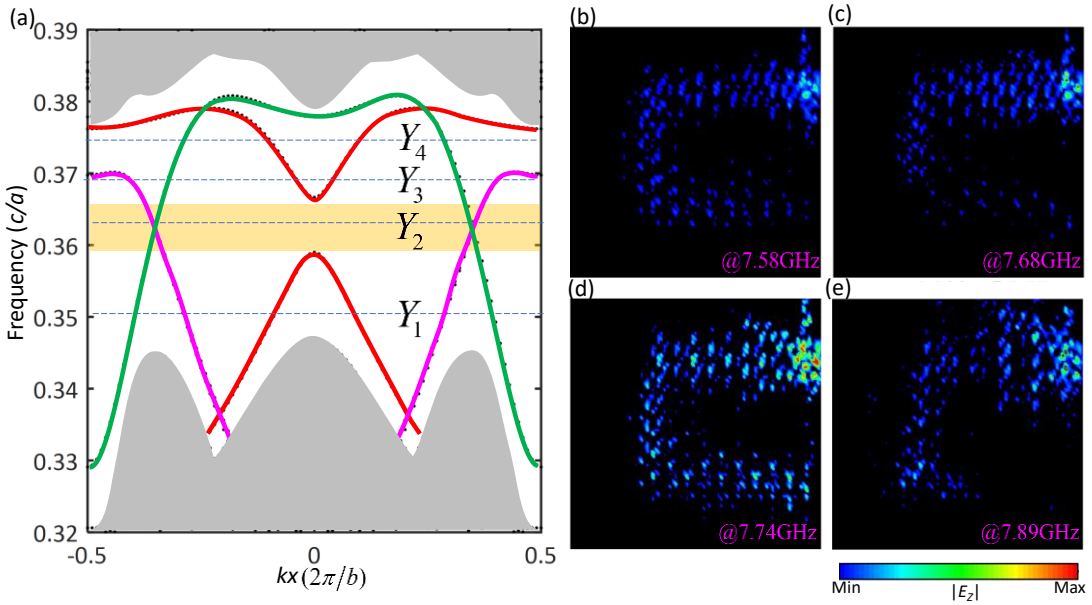

Figure S6. (a) Valley Hall edge modes dispersion curves of the bearded interface-1, -2 and armchair interface, marked by pink, green and red curves respectively. (b-e) Experimental observation for $|E_Z|$ distributions of U-shaped waveguide at different frequencies respectively.

6. Topological metasurface antenna

When the Bloch wave is coupled to the outer space, the refraction angles would take place change due to the near conservation of the valley DOF in momentum space. Here we further investigate applications in integrated photonics and on-chip communication, via constructing topological metasurface with different interfaces to realize various microwave antennas. The full field numerical simulation results are shown in Figure S7. When EMW transports through the bearded interface-1 and enter the air, the Bloch waves is divided into two beams of light along the black arrows, as shown in Figure S7(a2). The refraction angle is associated with the phase-matching conditions at the terminations [4]. While when EMW transports through the bearded interface-2 and enter the air, the EMW keeps straight transport along the black arrow without the refraction. The refraction angles are interpreted by the phase-matching conditions at the terminations, e.g., Figure S8(a) describes the ***k***-space analysis on the outcoupling of bearded interface. From which one can see that two solutions can be found with reflection symmetry about the *kx* axis. Similarly, when EMW transports through the comb-liked interface, zigzag interface, and armchair interface until enter the air, and the Bloch waves would transport along the black arrows in the air, as shown in Figures S7(c2-g2). In Figure S7(d2), the Bloch waves is divided into three beams of light along the black arrows and the refraction angles meet phase-matching conditions at the termination, which explained by the k-space analysis on the outcoupling of comb-liked interface-2 [see Figure S8(b)]. When EMW transports through the zigzag interface and enter the air, the refraction angles are different from the former ones. Why these cases are different from one another is that degree of coupling the symmetry of the VPC lattice and conservation degree of the valley DOF. The most importantly, for armchair interface, as shown in Figures S7(g2-g5), the interface symmetry (depended on δ) directly affects refraction direction, and valley Hall

edge states maintain transport along the zigzag interfaces without leaking of EMW into the air, indicating that valley Hall edge states in this case possess strong self-guided transmission [5].

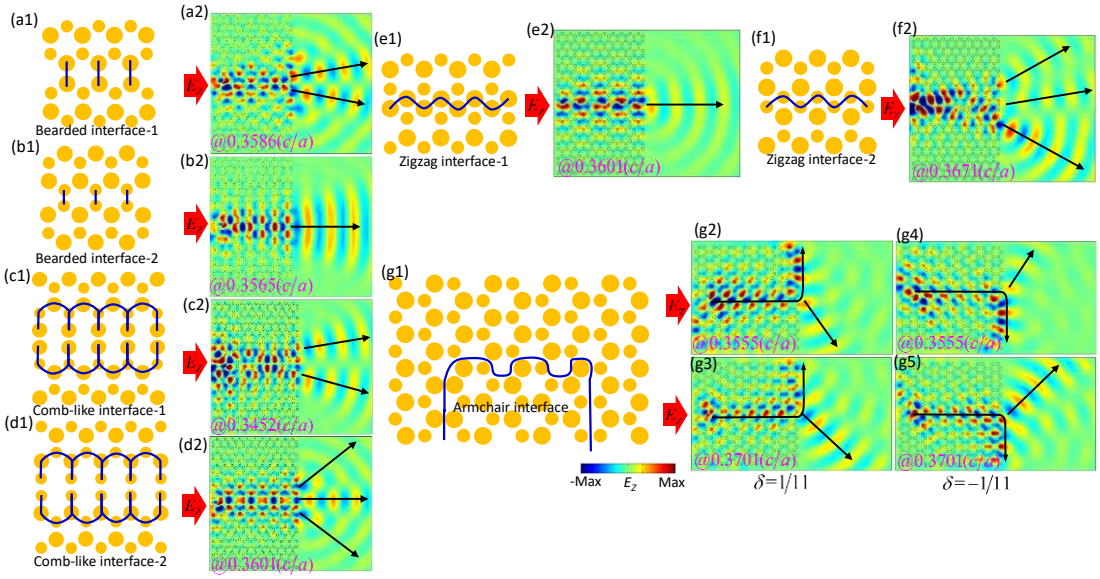

Figure S7. Electric field (E_Z) distributions of microwave antennas. (a1-g1) Schematic of different interface types. (a2-f2) E_Z distributions of valley Hall edge states through different interface types and air, where black arrows denote transport direction of EMW. (g2) and (g3) E_Z distributions of valley Hall edge states through armchair interface ($\delta = 1/11$) and air at different frequencies. (g4) and (g5) E_Z distributions of valley Hall edge states through armchair interface ($\delta = -1/11$) and air at different frequencies.

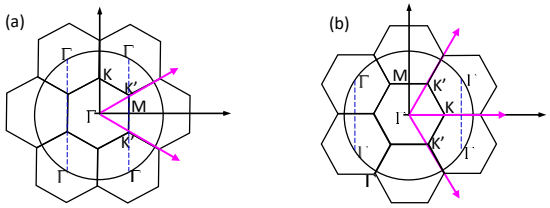

Figure S8. (a) and (b) The ***k***-space analysis on the outcoupling of (a) bearded interface and (b) comb-liked interface. Circles represent the dispersions of a free-space ***k*** vector. Pink arrows represent all possible outcoupling directions.

To further demonstrate transmission of topological metasurfaces antennas, we perform an experiment setup shown in Figures S9(a) and 9(d), aiming to observe EMW transport in topological metasurfaces. The VPCs are surrounded by absorbing materials (in blue) to avoid unwanted scattering, which is equivalent to scattering boundary condition in numerical simulations. The experimental results are shown in Figures S9(b), 9(c), 9(e) and 9(f). From which ones can see that when EMW transports through the bearded interface-1 and enter the air, EMW is divided into two beams of light along the pink arrows [see Figures S9 (c)]; while when EMW transports through the bearded interface-2 and enter the air, the EMW keeps straight transport along the pink arrow without the refraction, as shown in Figures S9(f). The experimentally observations are in line with previous discussions and analysis. The other experimental cases are not discussed here in repetition.

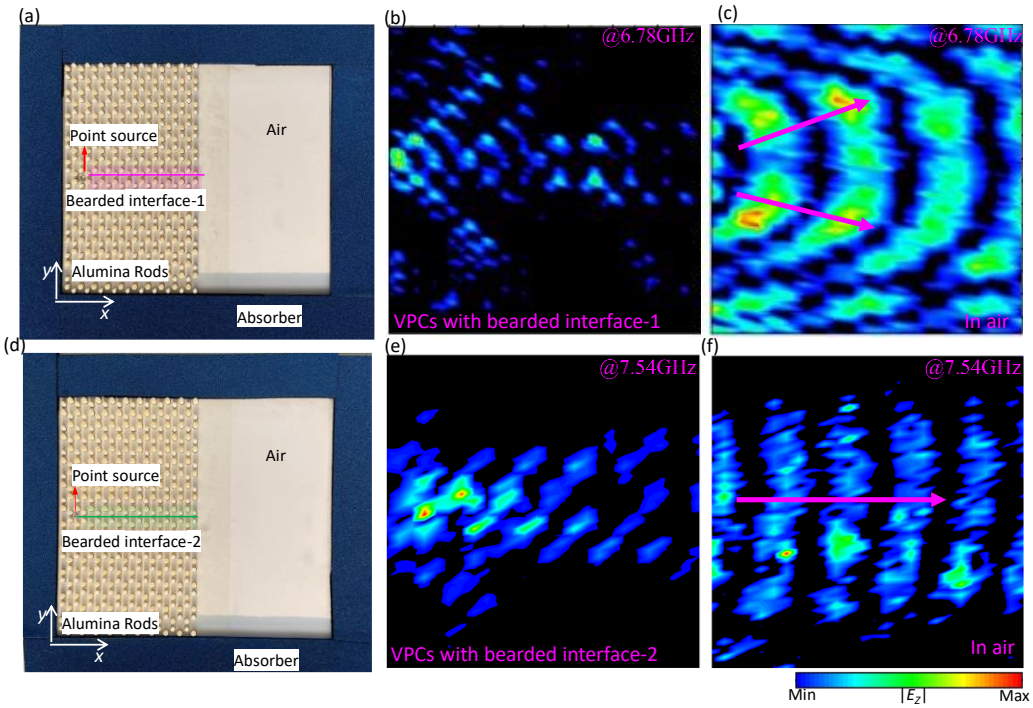

Figure S9. Experimental observation of microwave antennas. (a) and (d) Photograph of experimental samples from top view, the pink and green lines denote the bearded interface-1 and-2 respectively. All alumina cylinders are surrounded by microwave-absorbing foams (blue regions). (b) and (c) Experimental observation for $|E_Z|$ distributions of valley Hall edge states in the bearded interface-1 and air at frequency 6.78 GHz, where pink arrow denotes transport direction of EMW. (e) and (f) Experimental observation for $|E_Z|$ distribution of valley Hall edge states in the bearded interface-2 and air at frequency 7.54 GHz.

7. Method

Numerical simulations: Full wave simulations of this work are performed by the commercial finite element solver, COMSOL Multiphysics 6.0. To calculate the photonic band structures of the VPC unit cells in the first Brillouin zone, as shown in Fig. S1 in the Supplementary Material. Periodic boundary conditions are imposed on the opposite edges of the hexagonal unit cell. To calculate the projected photonic band structures along wavevector *kx* for different interfaces, periodic and perfect electric conductor boundary conditions are applied to the *x* and *y* directions of lattice supercell respectively, as shown in Figs. 2(b), 2(g) and so on. For full field numerical simulations of finite VPC structures, all computational domains are surrounded by scattering boundary conditions, as shown in Figs. 4(c1-c4) and so on. In numerical simulations data processing and analysis were performed in MATLAB. In simulation chiral source is constructed by three antennas with a phase difference of $2\pi/3$ between neighboring antennas along the anticlockwise or clockwise direction.

Experimental measurements: The VPC samples composed of alumina cylinders are assembled inside two parallel metallic plates, and transverse magnetic (TM) polarization is studied in the experimental measurements. In the microwave field mapper system, a chiral source is placed in the bottom plate through a drilled hole, and the time-harmonic field distributions are measured by a probing antenna connected to a vector network analyzer (Keysight E5063A) through the top metallic plate. To guarantee a smooth movement of the top plate in automatic measurements, there is a small air gap between alumina cylinders and the top plate. The electric field distributions are obtained by probe electromagnetic wave intensity, as shown in Figs.5(b-e) and Figure S9(b-e). The experimental data processing is performed in software Origin.

References

[1] Z. P. Qi, G. H. Hu, C. Y. Deng, *et al*., Electrical tunable topological valley photonic crystals for on-chip optical communications in the telecom band, *Nanophotonics*, vol. 11, no. 18, pp. 4273–4285, 2022.

[2] Q. L. Chen, L. Zhang, F. J. Chen, et al., "Photonic topological valley-locked waveguides," *ACS Photonics*, vol. 8, no. 5, pp. 1400-1406, 2021.

[3] H. S. Lai, H. Chen, B. He, *et al*., Symmetrical and anti-symmetrical topological edge states based on two-dimensional magneto-optical photonic crystals, *AIP Adv.*, vol. 10, no. 6, pp. 065029, 2020.

[4] B. Y. Xie, H. Liu, H. Cheng, *et al*., Acoustic topological transport and refraction in a Kekulé lattice, *Phys. Rev. Appl.*, vol. 11, no. 4, pp. 044086, 2019.

[5] Y. Poo, R. X. Wu, Z. F. Lin, *et al*., Experimental realization of self-guiding unidirectional electromagnetic edge states, *Phys. Rev. Lett.*, vol. 106, no. 9, pp. 093903, 2011.